PHYSICAL REVIEW C VOLUME 57, NUMBER 5 MAY 1998

^{19}Ne$(p,\gamma)^{20}$Na and ^{19}Ne$(d,n)^{20}$Na reactions and its astrophysical implications for the transition of the hot CNO cycle to the *rp* process

G. Vancraeynest, P. Decrock,* M. Gaelens, M. Huyse, and P. Van Duppen
Instituut voor Kern- en Stralingsfysica, University of Leuven, Celestijnenlaan 200 D, B-3001 Leuven, Belgium

C. R. Bain, T. Davinson, R. D. Page,† A. C. Shotter, and P. J. Woods
Department of Physics and Astronomy, University of Edinburgh, Edinburgh EH9 3JZ, United Kingdom

F. Binon, P. Duhamel, and J. Vanhorenbeeck
Institut d'Astronomie, d'Astrophysique et de Géophysique, Université Libre de Bruxelles, B-1050 Brussels, Belgium

R. Coszach, Th. Delbar, W. Galster, J. S. Graulich, P. Leleux, E. Liénard, P. Lipnik, C. Michotte,‡ A. Ninane, and J. Vervier
Institut de Physique Nucléaire, Université Catholique de Louvain, B-1348 Louvain-la-Neuve, Belgium

H. Herndl and H. Oberhummer
Institute of Nuclear Physics, Technical University of Vienna, Vienna, Austria

Cs. Sükösd
Institute of Nuclear Techniques, Technical University of Budapest, H-1521 Budapest, Hungary

M. Wiescher
Department of Physics, University of Notre Dame, Notre Dame, Indiana 46556

(Received 4 November 1997)

The population of the ^{20}Na resonances at 448, 661, 797, and 887 keV above the proton threshold has been studied in measurements of the ^{19}Ne$(p,\gamma)^{20}$Na reaction with radioactive ^{19}Ne beams. The data have been analyzed fully in terms of resonance strengths, enabling a comparison with theoretical estimates and the extraction of upper and lower limits on the resonant part of the ^{19}Ne$(p,\gamma)^{20}$Na astrophysical reaction rate. The total cross section of the ^{19}Ne$(d,n)^{20}$Na reaction has been measured from 0.6 to 1.8 MeV (c.m.). On the basis of the results of a subsequent distorted-wave Born approximation analysis the direct component of the ^{19}Ne$(p,\gamma)^{20}$Na astrophysical reaction rate has been calculated in a potential model. The astrophysical implications of the resulting total reaction rate have been investigated: the conditions for the breakout from the hot CNO cycle into the rapid-proton capture process are determined by the preceding ^{15}O$(\alpha,\gamma)^{19}$Ne reaction and the photodisintegration of the produced ^{20}Na nuclei will not impede the breakout. [S0556-2813(98)05305-9]

PACS number(s): 25.40.Lw, 25.45.Hi, 25.60.−t, 27.30.+t

I. INTRODUCTION

Explosive hydrogen burning [1–3] is thought to occur at various astrophysical sites in the Universe, either under degenerate conditions such as in novas and x-ray bursts, or under nondegenerate conditions such as in the shockwave of type-II supernovas passing through the hydrogen-rich outerlayer of the progenitor star and supermassive stars (the latter still being hypothetical). Typical values for temperature and density are indicated in Figs. 1 and 2.

At temperatures below 4×10^8 K the principal burning mode is the hot carbon-nitrogen-oxygen (CNO) cycle,

$$^{12}\mathrm{C}(p,\gamma)^{13}\mathrm{N}(p,\gamma)^{14}\mathrm{O}(\beta^+\nu)^{14}\mathrm{N}(p,\gamma)$$

$$^{15}\mathrm{O}(\beta^+\nu)^{15}\mathrm{N}(p,\alpha)^{12}\mathrm{C}.$$

Similar reaction cycles can, in principle, operate starting from heavier even-even $T_z=0$ nuclei and nuclear matter will leak from one cycle into the following depending on the ratio of the closing (p,α) reaction and the (p,γ) reaction on the $T_z=+1/2$ nucleus. However, an oxygen-fluor cycle starting from ^{16}O does not exist because already at the compound nucleus ^{19}Ne the α channel is open and the ^{18}F$(p,\alpha)^{15}$O reaction leads the flow back into the hot CNO cycle [4,5]. This effectively decouples the CNO region, containing the vast majority of nuclear matter, from the $A>20$ region and the sequence ^{16}O$(p,\gamma)^{17}$F$(p,\gamma)^{18}$Ne $(\beta^+\nu)^{18}$F$(p,\alpha)^{15}$O is considered as a sidebranch of the hot CNO cycle.

From temperatures of 3×10^8 K on, capture reactions involving β-unstable nuclei with long half-lives (''waiting points'') become important due to the faster time scale of the nuclear burning and the cycles break up and transform into

---

*Present address: Argonne National Laboratory, Physics Division, Bldg. 203, 9700 South Cass Avenue, Illinois 60439.

†Present address: Oliver Lodge Laboratory, University of Liverpool, Liverpool L69 3BX, UK.

‡Present address: Bureau International des Poids et Mesures, Section des Rayonnements Ionisants, 92310 Sèvres, France.

0556-2813/98/57(5)/2711(13)/$15.00

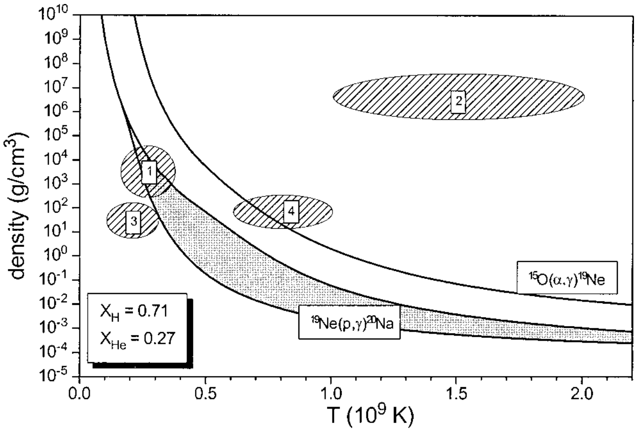

FIG. 1. A (density,temperature)-phase diagram of a stellar plasma with the solar composition. X_H and X_{He} stand for the hydrogen and helium mass fraction, respectively. The division between reaction-dominated (high ρ and T) and decay-dominated regions has been calculated for both ^{19}Ne(p,γ) and ^{15}O(α,γ) reactions. The gray band is due to the uncertainty on our ^{19}Ne$_{\mathrm{g.s.}}(p,\gamma)^{20}$Na astrophysical reaction rate (see Fig. 7). The hatched areas indicate typical values for temperature and density for explosive hydrogen burning in novas (1), x-ray bursts (2), type-II supernovas (3), and supermassive stars (4).

the *rp* process. In the case of the CNO cycle proton capture on ^{14}O, ^{15}O or ^{18}Ne leads to proton unbound nuclei, respectively, ^{15}F, ^{16}F, and ^{19}Na, nor can two-proton captures on these nuclei be of importance for realistic densities [6]. The CNO region remains decoupled from the *rp* process region, thereby preventing the onset of the *rp* process on a massive scale.

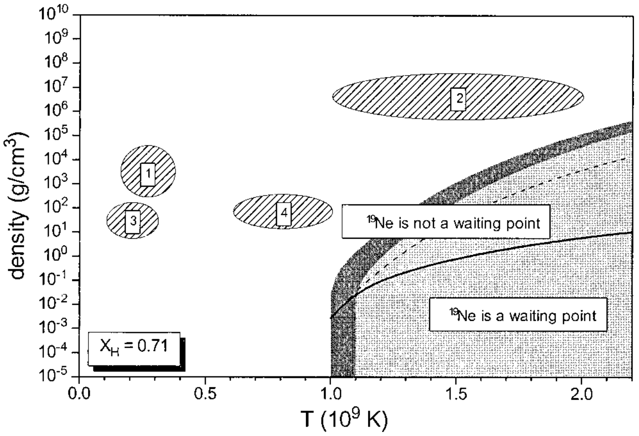

FIG. 2. A (density,temperature)-phase diagram of a stellar plasma with the solar composition. X_H and X_{He} stand for the hydrogen and helium mass fraction, respectively. The gray region indicates the conditions for which (p,γ)-(γ,p) equilibrium exists between ^{19}Ne and ^{20}Na. The dark gray band represents the uncertainty due to the uncertainty on our ^{19}Ne$_{\mathrm{g.s.}}(p,\gamma)^{20}$Na astrophysical reaction rate (see Fig. 7). The region in which ^{19}Ne is a waiting point due to the photodisintegration of ^{20}Na is delineated by the dashed line taking into account only the β^+ decay of ^{20}Na and by the full line taking into account the ^{20}Na$(p,\gamma)^{21}$Mg reaction in addition. The hatched areas indicate typical values for temperature and density for explosive hydrogen burning in novas (1), x-ray bursts (2), type-II supernovas (3), and supermassive stars (4).

One has to wait for the CNO cycle to open up until the temperature is high enough ($>4\times10^8$ K) for α-induced reactions to take place. It has been suggested that the link between the CNO cycle and the *rp* process is formed by the ^{15}O$(\alpha,\gamma)^{19}$Ne$(p,\gamma)^{20}$Na reaction sequence [1]. At still higher temperatures the ^{14}O$(\alpha,p)^{17}$F$(p,\gamma)^{18}$Ne$(\alpha,p)^{21}$Na reaction chain would form an alternative escape route [2,6]. The consequences of a breakout from the CNO cycle into the *rp* process are considerable. Large scale nucleosynthesis would take place up to $A=56$ and the energy generation would increase by two orders of magnitude compared to the hot CNO cycle [1]. The transition of the hot CNO cycle to the *rp* process has been proposed as a possible explanation of the observed overabundances of Ne and heavier elements up to S in nova ejecta [7] and of Ne and Na in cosmic rays [8].

The conditions of the breakout are determined by the weakest reaction of the escape sequence. In this light mass region the reactions are characterized by low Q values (a few MeV) and are dominated by single resonances, so that the knowledge of their individual properties (excitation energy, spin and parity, partial decay widths or resonance strength) is indispensable. In order to evaluate either reaction rate of the ^{15}O$(\alpha,\gamma)^{19}$Ne$(p,\gamma)^{20}$Na sequence one has had to rely on the properties of the (assumed) analog levels in the mirror nuclei, ^{19}F and ^{20}F, until now. Whereas the ^{15}O$(\alpha,\gamma)^{19}$Ne reaction rate is presumed to be known within a factor 2 [2]—an estimate that was borne out by later publications [9,10]—the situation is less favorable in the case of the ^{19}Ne$(p,\gamma)^{20}$Na reaction.

Figure 3 summarizes the current knowledge on the lower part of the ^{20}Na level scheme. Four resonances in ^{20}Na situated 448, 661, 797, and 887 keV[1] above the proton threshold at 2195 keV have been identified [11]. The states in ^{20}Na at 2992 and 3082 keV that correspond to the latter two have been unambigously assigned $J^\pi=1^+$ and $J^\pi=0^+$ in the resonant scattering of ^{19}Ne beams on a H target [12]. This is in agreement with the distorted-wave Born approximation (DWBA) analysis of the triton distributions of the ^{20}Ne$(^3$He$,t)^{20}$Na reaction [13,15] and the population of a level around 3 MeV in a Gamow-Teller (GT) transition in the β decay of ^{20}Mg [16–18]. The two levels are considered to be the mirrors of states in ^{20}F at 3488 and 3526 keV, respectively, and in ^{20}Ne at 13.484 and 13.642 MeV, respectively. The observed excitation energies in ^{20}Na are consistent with a shell-model calculation of the coefficients of the isobaric mass multiplet equation [13] and with calculated Coulomb shifts [19]. Furthermore the observed total widths in Ref. [12] agree with calculations based on these analog assignments (see Sec. III C).

However, the spin and parity and the identification of the mirror state in ^{20}F of the lowest, and therefore *a priori* most important, resonance and of the second lowest resonance are still subjects of debate. The state at 2643 keV corresponding to the 448 keV resonance has been observed in the

---

[1] We adopt the values from Görres and Wiescher [11], except for the fourth state because mutually inconsistent data have been averaged. We use the value from their reanalysis of the $(^3$He$,t)$ data of Lamm *et al.* [13] and from Coszach *et al.* [12].

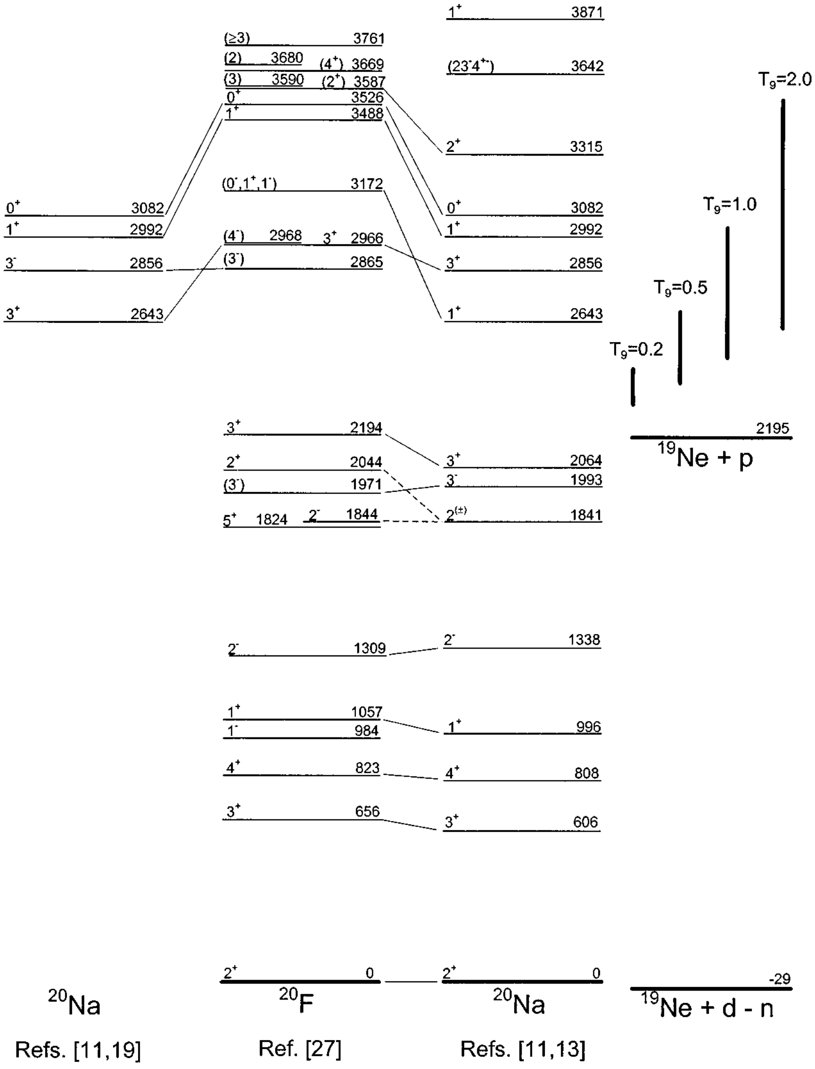

FIG. 3. Partial decay scheme of ^{20}Na and ^{20}F. The ground states have been put at the same height by convention. To the right of the ^{20}F levels the analog assignments according to Lamm *et al.* [13] are presented, to the left those according to Brown *et al.* [19]. The vertical lines at the very right represent the Gamow windows at the various temperatures indicated ($T_9=x$ means $T=x\times10^9$ K).

^{20}Ne(^{3}He,t)^{20}Na reaction [13–15,20–22] and in the ^{20}Ne$(p,n)^{20}$Na reaction at 30 MeV [15]. DWBA analysis of the triton and neutron distributions led to a 1^+ assignment. The level, however, was not observed in the β decay of ^{20}Mg which preferably populates $J^\pi=1^+$ states in GT transitions [16–18]. Furthermore in the ^{20}Ne$(p,n)^{20}$Na reaction at 135 MeV, which is also a sensitive test of the GT strength, the neutron distribution is characteristic for a $\Delta l=2$ transition without discernible $\Delta l=0$ component [23]. Both facts could be consistent with the identification of being the mirror state of the 3172 keV level in ^{20}F that was proposed by Lamm *et al.* [13]. This state had been assigned $J^\pi=1^+$ and had been identified as a $6p2h$ intruder state with little or no $4p0h$ mixing [24]. The characterization of this ^{20}F level is still tentative and the assignments $J^\pi=1^-$ [25] and $J^\pi=0^-$ [26,27] have also been proposed. The strength of the 448 keV resonance within the 1^+ assignment has been estimated by Lamm *et al.* [13] to be 6 meV. The level in ^{20}Na at 2856 keV corresponding to the 661 keV resonance is assigned $J^\pi=3^+$ and is considered the analog of the 2966 keV state in ^{20}F.

Brown *et al.* [19] question this characterization of the 2643 and 2856 keV levels. They note that the population of the 2643 keV level in the ^{20}Ne(^{3}He,t)^{20}Na is profoundly different from that of the 3172 keV level in the ^{20}Ne(t,^{3}He)^{20}F [28] and other transfer reactions. Moreover, the calculated Coulomb shift disagrees with the proposed analog assignment. By a process of elimination based on Coulomb shifts they arrive at the conclusion that the 2643 keV state in ^{20}Na most likely has $J^\pi=3^+$ and is the mirror of the 2966 keV state in ^{20}F. The nonobservation of the 2643 keV state in the β decay of ^{20}Mg [16–18] and the characteristic $\Delta l=2$ neutron distribution of the ^{20}Ne$(p,n)^{20}$Na reaction at high energies [23] are consistent with the proposed assignment. The strength of the 448 keV resonance within this assignment has been calculated in a shell model by Brown *et al.* [19] to be 80 meV. Likewise they conclude that the ^{20}Na state at 2856 keV has $J^\pi=3^-$ and is the mirror of the ^{20}F level at 2865 keV.

As for the direct capture (DC) into the bound states of ^{20}Na, Langanke *et al.* [29] also had to rely on information from the mirror nucleus ^{20}F in their evaluation of the DC rate. They used the neutron spectroscopic factors of the bound states in ^{20}F to rescale the DC rate obtained from the potential model by Rolfs [30].

Recently we have studied the population of the four lowest resonances in the ^{19}Ne$(p,\gamma)^{20}$Na reaction using ^{19}Ne beams at the Louvain-la-Neuve radioactive ion beam facility [31–33]. The experimental setups that have been used are reviewed in Sec. II and the normalization is discussed as well. In Sec. III the results are globally analyzed in terms of resonance strengths. On the one hand, this will allow us to compare them directly with theoretical estimates; on the other hand, lower and upper limits will be deduced for the resonant reaction rate (Sec. V B). In the same series of experiments the $^{19}\mathrm{Ne}(d,n)^{20}\mathrm{Na}$ excitation function in the energy domain from 0.6 to 1.8 MeV in center-of-mass (c.m.) system was measured [31–33]. In Sec. IV the DWBA analysis of our data is discussed and information on the proton spectroscopic factors of the lowest bound states, which are needed in a calculation of the DC rate, is extracted. A new calculation of the DC reaction rate in a potential model using a folding potential and the results of our DWBA analysis is presented in Sec. V A. In Sec. VI the astrophysical implications of the new total $^{19}\mathrm{Ne}(p,\gamma)^{20}\mathrm{Na}$ rate are investigated. A comparison with the $^{15}\mathrm{O}(\alpha,\gamma)^{19}\mathrm{Ne}$ is made and the effects of photodisintegration of the $^{20}\mathrm{Na}$ nuclei, which could be important at higher temperatures because of the low Q value of the $^{19}\mathrm{Ne}(p,\gamma)^{20}\mathrm{Na}$ reaction, are considered.

II. EXPERIMENTAL SETUPS AND DATA NORMALIZATION

The radioactive $^{19}\mathrm{Ne}$ ($T_{1/2}=17.2$ s) beam (typically 100 ppA) impinged on a polyethylene target foil or, in the case of the STAR-H_2 setup, on a closed gas cell filled with hydrogen gas. The advantages of a gas target are threefold. First, one does not have to care about the target stoichiometry. It is a well known fact that the proton content of the polyethylene foils, which we will denote by CH_x, gradually decreases during irradiation. Second, using depleted deuterium hydrogen gas one gets rid of the problem of parasitic counts due to the $^{19}\mathrm{Ne}(d,n)^{20}\mathrm{Na}$ reaction, which is 1000 to 10 000 times faster than the (p,γ) reaction. Third, the stopping of the beam is solely provided by the protons of the target so that the reaction yield is maximal. In the same series of measurements deuterated polyethylene foils, denoted by $\mathrm{CD}_x\mathrm{H}_y$, with typically 95% of the hydrogen being deuterium, or a gas cell filled with deuterium were used as a target in order to measure the total cross section of the $^{19}\mathrm{Ne}(d,n)^{20}\mathrm{Na}$ reaction over similar energy intervals as in the (p,γ) measurements.

Thanks to the inverse kinematics the $^{20}\mathrm{Na}$ nuclei that were produced were emitted in a narrow cone [$\theta<0.7°$ in the (p,γ) case, $\theta<4.2°$ in the (d,n) case at 19.2 MeV lab energy] and were implanted together with the beam. The subsequent β^+ decay or β^+-delayed α decay of the collected $^{20}\mathrm{Na}$ activity was detected in the presence of the huge positron background of the beam activity ($\sim 10^{12}$ positrons per $^{20}\mathrm{Na}$ ion). To that end three detection setups have been developed which have been described in detail elsewhere: (i) the detection of the β^+ decay ($E_\mathrm{e}=11.2$ MeV) by means of a stack of plastic scintillators located at the end of a solenoidal magnetic field that suppresses the low-energy positrons ($E_\mathrm{e}=2.2$ MeV) of the $^{19}\mathrm{Ne}$ decay (STAR-CH_x and STAR-H_2) [32–34], (ii) the detection of the β^+-delayed α line at 2.15 MeV (16.4% branching) by highly segmented double sided silicon strip detectors (DSSSD) [31] and (iii) by electrochemically etched solid state nuclear track detectors (SSNTD) [31–33,35].

The recorded $^{20}\mathrm{Na}$ signal was normalized by means of the recoil protons (deuterons) or scattered beam particles in the case of (deuterated) polyethylene target foils and by means of backscattered beam particles on a thin gold layer on the entrance window in the STAR-H_2 setup. The normalization spectra were registered in Si detectors. We deduced the average cross section using the following expressions in the case of a solid target or the gas cell, respectively:

$$\langle\sigma\rangle_\mathrm{solid}=\frac{N_\mathrm{reaction}}{\eta N_\mathrm{norm}}\frac{n_\mathrm{norm}}{n}\left\langle\frac{d\sigma}{d\Omega}\right\rangle d\Omega,$$

$$\langle\sigma\rangle_\mathrm{gas}=\frac{N_\mathrm{reaction}}{\eta N_{^{19}\mathrm{Ne}}}\frac{n_\mathrm{Au}d_\mathrm{Au}}{nd}\left\langle\frac{d\sigma}{d\Omega}\right\rangle d\Omega.$$

Here N_reaction is the number of counts originating from the $^{20}\mathrm{Na}$ nuclei produced in the reaction under study. η is the total efficiency of the setup, consisting of the detection efficiency, the branching of the specific decay mode one is registering and, in the DSSSD and SSNTD setups, the efficiency of transporting the $^{20}\mathrm{Na}$ activity to the detectors. N_norm is the number of scattered (or recoiling) particles registered in the monitoring Si detector. n_norm is the number density of target atoms active in this scattering and $\langle d\sigma/d\Omega\rangle$ is the scattering cross section averaged over the energy loss of the beam in the target and in the direction of the monitor detector which subtends a solid angle of $d\Omega$. n is the number density of target atoms active in the reaction under study (protons or deuterons). $N_{^{19}\mathrm{Ne}}$ is the number of beam particles in thenormalization spectrum that have backscattered on the gold layer on the entrance window of the gas cell. n_Au is the number density of Au atoms in the gold layer and d_Au its depth. d is the length of the gas cell.

The energy loss of the beam in the (deuterated) polyethylene target is easily deduced from the width of the proton (deuteron) peak in the normalization spectrum. For the gas target the energy loss is calculated from the length of the cell and the gas pressure.

In the case of the (p,γ) reaction using a polyethylene target N_reaction equals the $^{20}\mathrm{Na}$ signal S corrected for the number of counts due to the parasitic (d,n) reaction on naturally abundant (0.015%) deuterium in the CH_x target $N_1^{(d,n)}$:

$$N_\mathrm{reaction}=S-N_1^{(d,n)}.$$

The correction is obtained by rescaling the (d,n) reaction yield that was observed in a run on a $\mathrm{CD}_x\mathrm{H}_y$ target over a similar energy interval and could amount up to over 50% of the $^{20}\mathrm{Na}$ signal S. Using the thin target approximation (i.e., constant stopping power) and the Bragg rule for the stopping power in a compound [36], $N_1^{(d,n)}$ is given by

$$N_1^{(d,n)}=N_2^{(d,n)}\frac{1.5\times10^{-4}x_1}{x_2}\,\frac{\overline{\epsilon}_\mathrm{C}+(x_2+y_2)\overline{\epsilon}_\mathrm{H}}{\overline{\epsilon}_\mathrm{C}+x_1\overline{\epsilon}_\mathrm{H}}$$

$$\times\frac{\int_{\Delta_1}dE\,\sigma^{(d,n)}}{\int_{\Delta_2}dE\,\sigma^{(d,n)}}\,\frac{\eta_1}{\eta_2}\,\frac{D_1}{D_2}.$$

In this expression the subscripts 1 and 2 refer to the run with the CH_x target and with the $\mathrm{CD}_x\mathrm{H}_y$ target, respectively.

$N^{(d,n)}$ is the number of counts from the decay of ^{20}Na ions that have been produced by the ^{19}Ne(d,n) reaction. x_1 is the stoichiometric coefficient of the protons in the CH$_x$ target; x_2 (y_2) that of the deuterons (protons) in the CD$_x$H$_y$ target. The stoichiometry of the targets, which is initially CH$_2$ or CD$_x$H$_y$ with $x+y=2$, was monitored by plotting the proton and deuteron yields relative to a normalization parameter that was independent of the target stoichiometry, such as the scattered beam particles or the β^+ radioactivity of the beam. $\overline{\epsilon_C}$ and $\overline{\epsilon_H}$ is the stopping power of the beam in MeV/(atoms/cm^2) in, respectively, carbon and hydrogen, averaged over the energy loss of the beam in the respective targets. Δ represents the energy interval covered in the respective targets. The ratio of the integrals over Δ was evaluated with the use of the calculated DWBA (d,n) cross sections (see Sec. IV). The error on this ratio that is introduced by neglecting a possible compound nucleus contribution to the (d,n) reaction cross section is believed to be minor. D is the beam dose, i.e., a measure of the total number of beam particles incident on the target during the respective run.

Another complication using solid targets arose in the (d,n) measurements. Zabegai *et al.* [37] have measured the scattering of deuterium on ^{19}F, ^{23}Na, and $^{\mathrm{nat}}$Cl around and above the Coulomb barrier and have shown that it is influenced by elastic nuclear potential scattering. At sufficiently low energy and small c.m. angle the Rutherford scattering dominates. In the case of the ^{19}Ne$+^{12}$C scattering in our experiments the c.m. energy was at most 51% of the Coulomb barrier and the c.m. angle corresponding to the typical laboratory scattering angle into the monitor detector of 20° is only 53°, so that the ^{19}Ne$+^{12}$C scattering cross section can be assumed to be the Rutherford cross section. Comparing the yields in the monitor detectors of the recoiling deuterons and of the beam particles scattered on the carbon atoms of the target, we noticed, after correction for the target stoichiometry, that the ^{19}Ne$+d$ scattering cross section was less than the value for purely Rutherford scattering by a factor 0.6 ($E_{\mathrm{c.m.}}=1.83-1.70$ MeV) and 0.9 ($E_{\mathrm{c.m.}}=1.83-1.26$ MeV and $1.37-1.19$). For the measurements at lower energies the deuterium yields were consistent with purely Rutherford scattering. In the case of polyethylene targets the ^{19}Ne$+p$ scattering is not purely Rutherford either, but its cross section is well known [12].

III. THE STRENGTHS OF THE LOW-LYING ^{20}Na RESONANCES

A. The 448 keV resonance

The data collected by the DSSSD and the SSNTD setup have been presented in Ref. [31]. In the analysis of the SSNTD data an electronic effect had been overlooked that afflicted the spectra of the time of flight between the arrival of a particle in the monitor detector and the next cyclotron pulse. When the stop and start signal coming from constant fraction discriminators overlapped, the time-to-amplitude convertor (TAC) gave an output in channel 0. In that manner 8.2 ns of the 89.9 ns wide period of alternating voltage of the cyclotron was artificially compressed in channel 0. Now the correction for dead time and pile up was obtained by means of pulser:

$$\frac{P}{ftB},$$

with P the number of pulses in the energy spectrum gated on the TAC peak, $f=(2.03\pm0.06)$ Hz the pulser frequency, t the total time and B the ratio of the width of the TAC peak over the total width of the time spectrum. As a consequence the dead time and pile up correction was 9.8% too low and the SSNTD results in Ref. [31] should be multiplied by the factor 1.098, leading to a resonance strength of $\omega\gamma=14^{+12}_{-11}$ meV (upper limit 29 meV at 90% confidence level). Furthermore in the analysis of the DSSSD data the efficiency of transporting the ^{20}Na activity was 30.6% instead of 36% quoted in Ref. [31]. Therefore the DSSSD results in Ref. [31] should be multiplied by 1.18 (leading to an upper limit of $\omega\gamma\leqslant 24$ meV at 90% confidence level). The combination of both results yields a 90% confidence level upper limit of $\omega\gamma\leqslant 21$ meV.

B. The 661, 797, and 887 keV resonances

The population of the 661, 797, and 887 keV resonances in the ^{19}Ne$(p,\gamma)^{20}$Na reaction has been studied using the STAR-CH$_x$, the STAR-H$_2$ and the SSNTD setup and the data have been presented in terms of mean cross sections [32]. In order to make a sensible comparison with theoretical estimates of resonance strengths we have analyzed the data in terms of resonance strengths. Various combinations of the resonances have been measured (see Table I). The reaction yield that was determined for each measurement is a linear combination of the strengths of the resonances that were covered in the target. In the thin target approximation, which holds down to the percent level, and in the assumption that the resonant capture is the dominant reaction mechanism one has

$$\sum_i \lambda_{R_i}^2 C_i(\omega\gamma)_i = 2\langle\sigma\rangle\Delta E_{\mathrm{c.m.}}. \tag{1}$$

The right-hand side of this equation is a measure of the reaction yield with $\langle\sigma\rangle$ the experimental cross section averaged over the energy loss of the beam in the target and $\Delta E_{\mathrm{c.m.}}$ the center-of-mass value of this energy loss. The index i runs over the resonances. λ_R is the de Broglie wavelength at resonance energy. C is the coverage of a resonance in the target:

$$C=\int\int dx\,dy\frac{1}{\pi}\times\left(\arctan\frac{x-E_R}{\Gamma/2}-\arctan\frac{x-y-E_R}{\Gamma/2}\right)\times G(x,E_{\mathrm{in}},\Delta E_{\mathrm{in}})G(y,E_{\mathrm{loss}},\Delta E_{\mathrm{loss}}). \tag{2}$$

E_R is the resonance energy and Γ is the total width. $G(x,\mu,\sigma)$ stands for the Gaussian distribution of x with mean μ and standard deviation σ. E_{in} is the center-of-mass energy of the beam at the entrance of the target and ΔE_{in} the energy spread of the cyclotron beam, taken to be 0.6% [38] and, in the case of the gas target, augmented by the straggling in the nickel entrance window. E_{loss} is the center-of-

TABLE I. Overview of the results of the measurements on the 661, 797, and 887 keV resonances. $C_{x\ \mathrm{keV}}$ is the coverage in the target of the resonance at x keV above the proton threshold [see Eq. (2)].

Method	Center-of-mass energy interval covered in the target (MeV)	$C_{887\ \mathrm{keV}}$ [a]	$C_{797\ \mathrm{keV}}$ [b]	$C_{661\ \mathrm{keV}}$ [c]	$2\langle\sigma\rangle\Delta E_{\mathrm{c.m.}}$ ($10^4\,\mathrm{fm}^2\mathrm{meV}$)
STAR-H_2	0.92−0.55	0.70	0.96	1.00	8 ± 4
STAR-CH_x	0.97−0.63	0.91	0.96	1.00	50^{+20}_{-22} [d]
SSNTD	0.97−0.62	0.91	0.96	1.00	13 ± 9
STAR-CH_x	0.97−0.71	0.90	0.95	0.00	24^{+16}_{-18} [d]
SSNTD	0.97−0.73	0.89	0.93	0.00	7 ± 6
STAR-CH_x	0.73−0.52	0.00	0.00	1.00	2 ± 10

[a] We used $\Gamma=35.9$ keV [12].

[b] We used $\Gamma=19.8$ keV [12].

[c] Both values for the total width from Table II, $\Gamma=401$ eV and $\Gamma=0.33$ eV give the same result.

[d] An upper limit on the possible background from reactions on carbon producing β emitters [e.g., ^{12}C(^{19}Ne, ^{28}P)t] has been determined as $\leqslant 1\times10^5$ fm^2 meV for the thick target and $\leqslant 8\times10^4$ fm^2 meV for the thin target. This has been taken into account as a one-sided negative contribution to the systematic uncertainty [32].

mass energy loss of the beam in the target and ΔE_{loss} is the energy straggling. Table I gives an overview of our measurements in terms of the quantities introduced in Eq. (1). The determination of the resonance strengths can be viewed as solving an overdetermined system of linear equations in the resonance strengths. After equilibration of the system the least-squares approximation did not lead to a sensible solution, as could have been expected because the problem is badly conditioned in the technical meaning of the word. Therefore we focused on the group of measurements in which the three resonances had been covered and which had led to a result significantly different from zero [32]. For each of the three measurements separately (rows 1 to 3 in Table I) Eq. (1) was solved as if all the measured strength had been concentrated on the 887 keV resonance. The weighted mean of the three solutions equals (152 ± 53) meV. The same procedure was followed for the 797 keV resonance and for the 661 keV resonance yielding values of, respectively, (102 ± 36) and (81 ± 29) meV. This analysis leads to the equation of a plane in the $(\omega\gamma_{887\ \mathrm{keV}},\omega\gamma_{797\ \mathrm{keV}},\omega\gamma_{661\ \mathrm{keV}})$ space which contains the true resonance strengths, expressed in meV (Fig. 4):

$$\frac{\omega\gamma_{887\ \mathrm{keV}}}{152\pm53}+\frac{\omega\gamma_{797\ \mathrm{keV}}}{102\pm36}+\frac{\omega\gamma_{661\ \mathrm{keV}}}{81\pm29}=1. \tag{3}$$

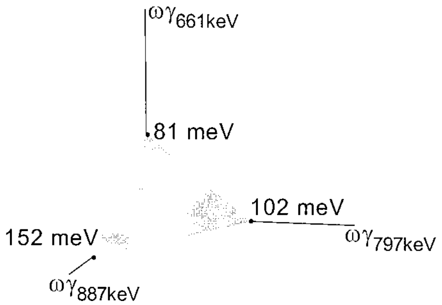

FIG. 4. Plane in the $(\omega\gamma_{887\ \mathrm{keV}},\omega\gamma_{797\ \mathrm{keV}},\omega\gamma_{661\ \mathrm{keV}})$ space that contains the true triple of resonance strengths, expressed in meV.

As a consequence the *sum* of the three resonance strengths, in meV, must lie between

$$81\pm29\leqslant\omega\gamma_{887\ \mathrm{keV}}+\omega\gamma_{797\ \mathrm{keV}}+\omega\gamma_{661\ \mathrm{keV}}\leqslant152\pm53. \tag{4}$$

C. Comparison with theoretical estimates

The strength of a ^{20}Na resonance for proton capture by ^{19}Ne in its ground state ($J^\pi=1/2^+$) is given by

$$\omega\gamma=\frac{2J_f+1}{4}\,\frac{\Gamma_{p_0}\Gamma_\gamma}{\Gamma}, \tag{5}$$

with J_f the spin of ^{20}Na resonance. The total width Γ of each ^{20}Na resonance under consideration is composed of the partial width for γ decay and the partial widths for proton decay to the ground state (Γ_{p_0}) and the first (Γ_{p_1}) and second (Γ_{p_2}) excited state in ^{19}Ne, respectively, at $E_x=238$ keV ($J^\pi=5/2^+$) and $E_x=275$ keV ($J^\pi=1/2^-$):

$$\Gamma=\Gamma_\gamma+\Gamma_{p_0}+\Gamma_{p_1}+\Gamma_{p_2}.$$

Within the two schemes of assignments for the 448, 661, 797, and 887 keV resonances that have been proposed, either by Lamm *et al.* [13] or by Brown *et al.* [19] (see Fig. 3), we have calculated the resonance strengths in a consistent way.

Single-particle proton widths were obtained in the framework of elastic scattering from a folding potential which is given by [39,40]

$$V(R)=\lambda\int\int d\mathbf{r}_1 d\mathbf{r}_2\ \rho_a(\mathbf{r}_1)\rho_A(\mathbf{r}_2)v_{\mathrm{eff}}(E,\rho_a,\rho_A,s), \tag{6}$$

where λ is a potential strength parameter close to unity and $s=|\mathbf{R}+\mathbf{r}_2-\mathbf{r}_1|$ with R denoting the separation of the centers of mass between projectile and target. The density distributions ρ_a and ρ_A of projectile and target can be deduced from

TABLE II. Estimates for the resonance strengths for proton capture on ^{19}Ne$_{\mathrm{g.s.}}$. Unless stated otherwise, the estimates are based on shell-model calculations (see text).

E_R (keV)	J^π	Γ_γ (meV)	Γ_{p_0} (eV)	Γ_{p_1} (eV)	Γ_{p_2} (eV)	Γ (eV)	$\omega\gamma$ (meV)
448	1^+ [13]	9.3 [a]	0.083 [b]	$\ll\Gamma_{p_0}$ [b]	$\ll\Gamma_{p_0}$ [b]	0.092	6
	3^+ [19]	123	0.75	0.95	$\ll\Gamma_{p_0}$	1.82	89
661	3^+ [13]	164	14	387	$\ll\Gamma_{p_0}$	401	10
	3^- [19]	23 [c]	0.016	0.275	0.0196	0.33	2
797	1^+	47	13×10^3	$\ll\Gamma_{p_0}$	$\ll\Gamma_{p_0}$	13×10^3	35
887	0^+	107	35×10^3	$\ll\Gamma_{p_0}$	$\ll\Gamma_{p_0}$	35×10^3	27

[a] Taken from [13].

[b] Calculated using the neutron spectroscopic factors of the 3172 keV 1^+ level in ^{20}F from [43].

[c] Deduced from the measured lifetime of the 2865 keV state in ^{20}F: (29 ± 4) fs [27].

measured charge-density distributions [41] or from nuclear structure models like Hartree-Fock calculations. The effective nucleon-nucleon interaction v_{eff} was taken from the DDM3Y parametrization [40]. The same folding potential was used in the calculation of DC reaction rate (Sec. V A). The strength parameter λ was adjusted to reproduce the respective resonance energies.

These single-particle widths were then scaled by spectroscopic factors that were calculated using the shell-model code OXBASH [42]. The spectroscopic factors for the 448 keV resonance could not be calculated if the level is characterized as a $6p2h$ intruder state [13]. In that case we relied on the experimental neutron spectroscopic factors of the proposed mirror in ^{20}F [43].

For γ decays proceeding predominantly through $M1$ and $E2$ transitions we have calculated the γ-decay widths within the shell model, which is expected to yield reliable predictions [27]. The γ widths are deduced from the electromagnetic transition probabilities $B(J_i\rightarrow J_f,L)$ which are calculated from the shell-model wave functions. We use the effective charges and g values obtained in Refs. [44,45].

In two cases the γ decay is dominated by $E1$ transitions. For the 448 keV resonance in the 1^+ assignment of Lamm *et al.* we have adopted the estimate from Ref. [13]. For the 661 keV resonance in the 3^- assignment of Brown *et al.*, the γ decay width was deduced from the recently measured lifetime of the proposed mirror state at 2865 keV in ^{20}F of (29 ± 4) fs [27]. We corrected for the E_γ^3 dependence according to the branchings for the different γ lines, for which we took the values for the 2865 keV state in ^{20}F [27].

The resulting estimates are presented in Table II. The calculated widths for the 797 and 887 keV resonances agree with the measured values in the ^{19}Ne$+p$ scattering [12] of (19.8 ± 2) keV and (35.9 ± 2) keV, respectively. As for the resonance strengths, a clearly different estimate for the strength of the lowest resonance appears for a $J^\pi=1^+$ or for a $J^\pi=3^+$ assignment, 6 and 89 meV, respectively. The sum of the strengths of the 661, 797, and 887 keV resonances is more or less the same in both assignment schemes, 72 and 64 meV, respectively.

Our 90% confidence upper limit of $\omega\gamma\leqslant21$ meV for the 448 keV resonance is well below the estimates for the 3^+ assignment [19] from Table II, whereas it is compatible with the estimates for the 1^+ intruder assignment [13]. Our limits on the sum of the strengths of the three highest resonances [see Eq. (4)] are consistent with the estimates in both schemes of assignments, although the estimates appear to be on the low side compared to our data.

IV. THE DWBA ANALYSIS OF THE ^{19}Ne$(d,n)^{20}$Na EXCITATION FUNCTION

We have probed the ^{19}Ne$(d,n)^{20}$Na excitation function over a center-of-mass energy range from 0.63 to 1.84 MeV in various measurements using the different experimental setups [31,32]. In that way up to the fourth excited level in ^{20}Na was populated (see Fig. 3). The data, represented in Fig. 6, are in good agreement with each other.

In order to extract information on the spectroscopic factors of the bound states that were populated in our measurements, we have performed a DWBA analysis of the experimental excitation curve. In the DWBA formalism the differential cross section of a transfer reaction $a+A\rightarrow b+B$ is given by

$$\frac{d\sigma}{d\Omega}=\frac{\mu_{aA}\mu_{bB}}{(2\pi\hbar)^2}\frac{k_\beta}{k_\alpha}\frac{1}{(2J_a+1)(2J_A+1)}\times\sum_{M_aM_AM_bM_B}|T(\mathbf{k}_\alpha\mathbf{k}_\beta)|^2. \tag{7}$$

In this equation μ_{aA}, μ_{bB}, k_α and k_β represent the reduced masses and the wave numbers in the entrance and exit channel, respectively. The transition amplitude is defined as

$$T(\mathbf{k}_\alpha,\mathbf{k}_\beta)=\int\int d\mathbf{R}d\mathbf{r}\chi^{-*}(\mathbf{k}_\beta,\mathbf{r}_{bB})\times\langle\psi_b\psi_B|V|\psi_a\psi_A\rangle\chi^+(\mathbf{k}_\alpha,\mathbf{r}_{aA}). \tag{8}$$

The wave functions ψ_a, ψ_A, ψ_b, and ψ_B are the internal wave functions of the respective nuclei.

In a stripping reaction the nucleon group x is transferred from the projectile a to the nucleus A to form the final nucleus B. In that case the integration has to be performed over the center-of-mass coordinates $\mathbf{R}$ of the nucleon group x and the relative coordinates $\mathbf{r}$ between the group x and ejectile b.

The optical wave functions χ^+ and χ^- are obtained from the optical potential which can be a Woods-Saxon potential

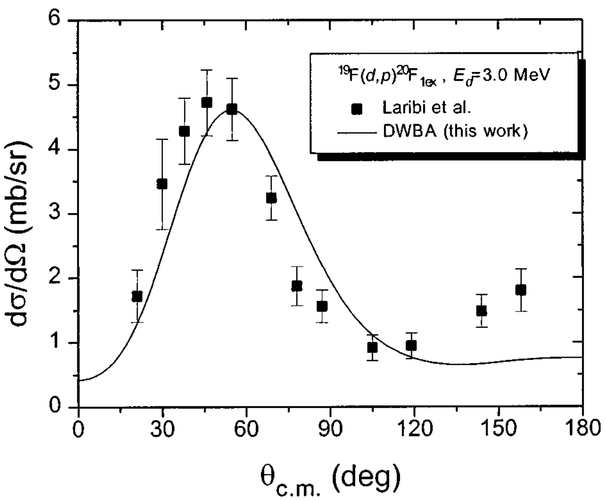

FIG. 5. Differential cross section for the $^{19}\mathrm{F}(d,p)\,^{20}\mathrm{F}_{1\mathrm{ex}}$ reaction at 3.0 MeV deuteron energy. Our DWBA calculation, using the shell-model spectroscopic factor of 0.63 for the first excited state in ^{20}F, is compared with the experimental data of Laribi *et al.* [48].

or a folding potential. The proper choice of the optical potential is a very important point in the DWBA calculation.

In order to determine the deuterium potential in the entrance channel $^{19}\mathrm{Ne}+d$, we first investigated the mirror reaction $^{19}\mathrm{F}(d,p)\,^{20}\mathrm{F}$. This reaction has been measured and calculated by several authors. At low deuteron energies this was done in Refs. [46–48]. It was found that many of the final states are predominantly populated via a compound nucleus formation. The spectroscopic factors to most final states are very small which suppresses the direct mechanism. However, for the first excited state in ^{20}F, the 3^+ state at 656 keV, the spectroscopic factor is high and the stripping reaction proceeds clearly in the direct mechanism. The angular distribution of this transition was reproduced nicely in the previous calculations [46–48]. The transition to this state accounts for about 60% of the observed overall population up to the fifth excited ^{20}F state. The latter is the mirror of the highest lying level in ^{20}Na that had been populated in our $^{19}\mathrm{Ne}(d,n)^{20}\mathrm{Na}$ experiments (see Fig. 3).

In our DWBA analysis of the $^{19}\mathrm{F}(d,p)\,^{20}\mathrm{F}$ angular distributions of Refs. [46–48] the best results were obtained with a Woods-Saxon potential in the entrance channel having the following parameters: $V_R=98$ MeV, $r_R=1.0$ fm, $a_R=0.8$ fm for the real part and $W_S=12$ MeV, $r_S=1.37$ fm, $a_S=0.7$ fm for the imaginary surface part. This potential is almost identical with the potential of Ref. [47]. In the exit channel we used the same folding potential as for the $^{19}\mathrm{Ne}(d,n)^{20}\mathrm{Na}$ reaction. This potential will be discussed later. The bound state potential is a real Woods-Saxon potential with $r_R=1.07$ fm and $a_R=0.74$ fm. The potential depth is adjusted to give the correct binding energy.

With these potentials we were able to reproduce the low-energy differential cross section for the transition to the first excited state in the $^{19}\mathrm{F}(d,p)\,^{20}\mathrm{F}$ reaction. In Fig. 5 the differential cross section of $^{19}\mathrm{F}(d,p)\,^{20}\mathrm{F}_{1\mathrm{ex}}$ at an incident energy of $E_\mathrm{d}=3.0$ MeV is displayed. Our DWBA calculation, using the shell-model spectroscopic factor of 0.63, is compared with the measured cross section of Laribi *et al.* [48]. Besides this we also found good agreement with the results of Ref. [47] for the transition to the first excited state. Due to the compound character of the transitions to the other states the angular distributions could not be reproduced. We concluded that the same deuteron potential could be used to obtain the direct contribution of the reaction $^{19}\mathrm{Ne}(d,n)^{20}\mathrm{Na}$.

In the exit channel $^{20}\mathrm{Na}+n$ we used a folding potential. Since no neutron-scattering data of ^{20}Na are available we used the thermal scattering cross section of ^{23}Na to determine the potential depth [49]. We assumed that the volume integral per nucleon for neutron scattering is approximately constant for an isotope chain. With this assumption we obtained the strength parameter λ for ^{20}Na from the optical potential of ^{23}Na.

The bound state potential in ^{20}Na that we used in the analysis of the $^{19}\mathrm{Ne}(d,n)^{20}\mathrm{Na}$ data was a Coulomb potential with $r_C=1.2$ fm and a real Woods-Saxon potential with $r_R=1.07$ fm and $a_R=0.74$ fm. The depth of the latter was adjusted to reproduce the respective binding energies.

Having determined the potentials we calculated the DWBA cross section to the bound states of ^{20}Na that had been populated in our experiments. Since it is not possible to extract unambiguously the respective spectroscopic factors from a DWBA fit to the experimental excitation curve, we had to rely either on neutron spectroscopic factors of the mirror states in ^{20}F or on the shell-model values [42]. Several authors have deduced neutron spectroscopic factors from the $^{19}\mathrm{F}(d,p)\,^{20}\mathrm{F}$ reaction. Laribi *et al.* [48] obtained a spectroscopic factor of 0.68 for the transition to the first excited state. Comsan *et al.* [47] give two values, averaged over different incident energies, depending on the choice of potential: 0.57 ± 0.05 and 0.68 ± 0.12. The shell-model calculation gives a spectroscopic factor of 0.63 in agreement with these results (see also Fig. 5). The data of Fortune *et al.* [43] obtained at higher deuteron energy, have also been reproduced with our DWBA calculation revealing a spectroscopic factor of 0.50. In our calculation of the $^{19}\mathrm{Ne}(d,n)^{20}\mathrm{Na}$ excitation function we therefore used the shell-model spectroscopic factors.

The transition to the first excited 3^+ state at 606 keV contributes 90% of the overall direct cross section for transitions up to the fourth excited state. In Fig. 6 the DWBA total cross section is compared with the experimental data. Also shown is the DWBA cross section multiplied with an overall scaling factor of 1.25, which resulted from a fit of the calculated DWBA cross section averaged over the experimental energy intervals to the data. This scaling factor can be explained by the probable contributions of compound nucleus (CN) reactions. We assume that, like in the analog reaction $^{19}\mathrm{F}(d,p)\,^{20}\mathrm{F}$, the transition to the other states is dominated by the CN mechanism.

We conclude that the most important contribution to the cross section of the reaction $^{19}\mathrm{Ne}(d,n)^{20}\mathrm{Na}$ is the direct transition to the first excited state ($\approx$ 70%), while the direct reaction to the other states amounts to strictly less than 10% of the total cross section. The remaining contributions are transitions to the other states by a CN mechanism. Following this argumentation we do not renormalize the spectroscopic factors in order to achieve the best possible agreement with the experiment. We will use the same shell-model spectroscopic factors for the capture reaction in the following paragraph.

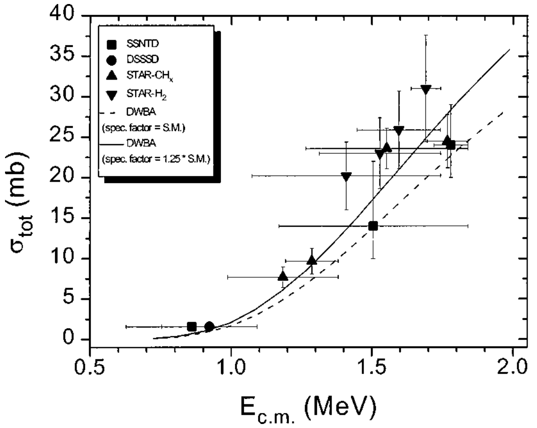

FIG. 6. ^{19}Ne$(d,n)^{20}$Na excitation function measured with the different setups. The horizontal bars represent the energy intervals that were covered in the respective measurements. The dashed curve is our DWBA calculation using the shell-model (S.M.) values of the spectroscopic factors of the states in ^{20}Na that were populated. The full curve is the DWBA excitation function after fitting an overall multiplication factor of 1.25.

V. THE ^{19}Ne$(p,\gamma)^{20}$Na ASTROPHYSICAL REACTION RATE

From our measurements, limits for the ^{19}Ne$(p,\gamma)^{20}$Na astrophysical reaction rate with ^{19}Ne in its ground state can be deduced.

A. The direct capture rate

We calculate the direct capture cross sections for transitions to all bound states of ^{20}Na. The total direct cross section is then given by the sum over all transitions, weighted by the spectroscopic factors:

$$\sigma_{\text{tot}}^{\text{DC}} = \sum_i (C^2S)_i \sigma_i^{\text{DC}}. \tag{9}$$

In general, only E1 transitions have to be considered.

The potential in the entrance channel is a folding potential. Since no experimental data are available to adjust the strength parameter λ, we chose the thermal neutron-scattering cross section of ^{19}F [49] to determine the potential depth. Hereby we assume that the volume integral per nucleon of the optical potential of ^{19}F$+n$ is the same as for ^{19}Ne$+p$. The bound state potential is the same folding potential but with the depth adjusted to reproduce the respective proton binding energies.

With a shell-model spectroscopic factor of 0.63 the capture to the first excited state contributes more than 60% to the direct capture cross section. The transition to the mirror of the 2044 keV 2^+ state in ^{20}F, which we assumed to be contained in the $J^\pi = 2^{(\pm)}$ level in ^{20}Na at 1841 keV excitation energy (see Fig. 3), makes up approximately 25% of the direct capture since the spectroscopic factor of this state is quite high (0.73).

The astrophysical S factor for the total direct capture reaction can be parametrized as

$$S_{\text{DC}}(E) = 1.0025 + 0.2288E + 0.0688E^2 \quad (\text{keV b}). \tag{10}$$

With this S factor we evaluate the direct capture part of the reaction rate as

$$\begin{aligned} N_{\text{A}}\langle\sigma v\rangle_{\text{DC}} = {} & 1.72\times 10^7 T_9^{-2/3}\{1 + 0.021\,5T_9^{1/3} + 0.127T_9^{2/3} \\ & + 0.019\,1T_9 + 0.021\,3T_9^{4/3} + 0.008\,14T_9^{5/3}\} \\ & \times\exp(-19.386T_9^{-1/3})(\text{cm}^3\ \text{s}^{-1}\ \text{mol}^{-1}). \end{aligned} \tag{11}$$

Compared to the direct capture rate calculated by Langanke *et al.* [29] our rate is one order of magnitude larger. This difference is partly explained by the fact that Langanke used the spectroscopic factors of Ref. [43] which are smaller by a factor of 2. Moreover he did not include the strong $p\rightarrow d$ wave component in the direct capture of the first excited state at 0.606 MeV (3^+) in ^{20}Na. This transition carries the dominant fraction of the total cross section because of the large spectroscopic factor of the final state. The present direct capture rate is therefore larger by about a factor of 5 compared to the previous estimate [29].

The calculated DC cross section can be used to extract the DC cross section averaged over the energy intervals that had been covered in our (p,γ) measurements. In the experiments in which the 661, 797, and 887 keV resonances have been covered, the average DC cross section is 33 nb, indicating that our measured cross section, (1.6 ± 0.7) μb [32], is clearly of resonant origin. The average DC cross section in our measurements of the 448 keV resonance is calculated to be 2.7 nb.

B. The resonant reaction rate

Both upper and lower limits on the resonant reaction rate have been deduced using the narrow resonance formalism, in which the reaction rate for a single resonance is given by

$$N_A\langle\sigma v\rangle_R = N_A\left(\frac{2\pi}{\mu kT}\right)^{3/2}\hbar^2\omega\gamma\exp(-E_R/kT). \tag{12}$$

The reaction rate for several narrow resonances is the sum of the respective rates.

The upper limit for the strength of the 448 keV resonance gives an upper limit on its contribution to the reaction rate. The upper and lower limit on the *sum* of the contributions from the 661, 797, and 887 keV resonances is obtained as follows. Three fictitious rates were calculated as if all the strength was concentrated in one of the three resonances using as a value for the resonance strength the intersection of the plane given by Eq. (3) and the respective axis in the $(\omega\gamma_{887\text{ keV}}, \omega\gamma_{797\text{ keV}}, \omega\gamma_{661\text{ keV}})$ space: 152, 102, 81 meV, respectively, (see Fig. 4). Because the *sum* of the contributions from the 661, 797, and 887 keV resonances to the reaction rate is a linear function of the reaction strengths and because the reaction strengths are constrained by a linear relation, Eq. (3), the true value of this sum always lies between the lowest and highest one of these three fictitious curves. In that way below $T = 4.1\times 10^9$ K the upper limit on the *sum* of reaction rates due to the three resonances under consideration is given by the reaction rate for the 661 keV resonance with a (fictitious) strength of 81 meV. Below T

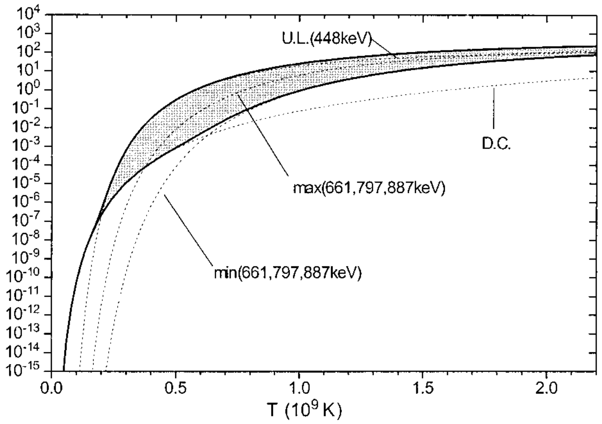

FIG. 7. The astrophysical reaction rate for the $^{19}\mathrm{Ne}_{\mathrm{g.s.}}(p,\gamma)\,^{20}\mathrm{Na}$ reaction resulting from our work. The limits on the total reaction rate are indicated by thick lines. In dashed lines the separate component reaction rates are shown (see text).

$=2.6\times10^9$ K the lower limit is given by the reaction rate for the 887 keV resonance using a (fictitious) strength of 152 meV.

In the case of the 797 or 887 keV resonance the narrow resonance formalism is not valid below $T=5\times10^8$ K. The integral of σv over the Maxwell-Boltzmann velocity distribution is dominated by the Gamow peak situated at the low energy side of the resonance and not by the resonance itself. As a consequence the approximation on which Eq. (12) is based, is not valid any more and the integral over the velocity distribution has to be evaluated explicitly. However, in the low-temperature domain upper and lower limits of the total reaction rate are dominated by the DC and the narrow 448 keV resonance (see Fig. 7), so that this consideration is not relevant in the evaluation of the *total* reaction rate.

C. The total reaction rate

The broad resonances at 797 and 887 keV above the threshold do not mutually interfere as they have a different spin [50]. Focusing on $E1$ transitions in the DC model, interference of these s-wave resonances and the direct capture requires an $s\rightarrow p$ transition. A few bound states in ^{20}Na with p-wave character exist, but the DC population of these negative parity states is small due to their small spectroscopic factor. Interference of the direct capture with the 797 and 887 keV resonances we therefore believe to be negligible. Interference effects involving the 448 and 661 keV resonances, if possible, are negligible due to their narrow widths. Therefore the total reaction rate is merely the sum of the resonant and DC components.

The lower limit on the total reaction rate is obtained by making the sum of the DC rate and the lower limit on the sum of the contributions from the 661, 797, and 887 keV resonances. This approach corresponds to putting the lower limit on strength of the 448 keV resonance to zero. The upper limit on the total rate is the sum of the DC rate and the upper limit on the resonant rate. The latter in its turn is the sum of the upper limits on the contribution of the 448 keV resonance and on the sum of the contributions from the three higher resonances. The limits on the total reaction rate, indicated by thick lines, are displayed in Fig. 7, together with the separate component reaction rates.

The reaction rate in Fig. 7 is based on our experimental results and is therefore valid for the case of all ^{19}Ne nuclei being in the ground state. The ^{20}Na resonances that we have considered could also be populated from the first and second excited states in ^{19}Ne at 238 and 275 keV excitation energy.

The time scale of the photoexcitation–de-excitation process in the hot photon bath in the star is, except for long-lived isomeric states, much shorter than the hydrodynamical time scale of the astrophysical process, even in explosive conditions [51]. The fraction P_j of ^{19}Ne nuclei in the jth excited state at excitation energy E_{x_j} can then be calculated under the assumption of thermal equilibrium and is given by

$$P_j=\frac{(2J_j+1)\exp(-E_{x_j}/kT)}{Z} \tag{13}$$

with Z the partition function:

$$Z=\sum_i (2J_j+1)\exp(-E_{x_j}/kT).$$

The reaction rate is then a weighted sum over the contributions due to the different excited states of ^{19}Ne, $\langle\sigma v\rangle_j$:

$$N_A\langle\langle\sigma v\rangle\rangle=\sum_j P_j N_A\langle\sigma v\rangle_j . \tag{14}$$

In the narrow resonance approximation the resonant reaction rate with ^{19}Ne in its jth excited state is given by

$$N_A\langle\sigma v\rangle_{R_j}=N_A\langle\sigma v\rangle_{R_0}\frac{2J_0+1}{2J_j+1}\frac{\Gamma_{p_j}}{\Gamma_{p_0}}\exp(+E_{x_j}/kT).$$

$N_A\langle\sigma v\rangle_{R_0}$ is the resonant reaction rate with ^{19}Ne in its ground state, given by Eq. (12) with $\omega\gamma$ the resonance strength for proton capture by ^{19}Ne in its ground state [Eq. (5)]. The summation in Eq. (14) only runs up to the second excited state in ^{19}Ne, because the third excited state is situated at 1508 keV excitation energy. The resonant $^{19}\mathrm{Ne}(p,\gamma)$ reaction rate in the narrow resonance formalism then becomes

$$N_A\langle\langle\sigma v\rangle\rangle_R=N_A\langle\sigma v\rangle_{R_0}\frac{2J_0+1}{Z}\left(1+\frac{\Gamma_{p_1}}{\Gamma_{p_0}}+\frac{\Gamma_{p_2}}{\Gamma_{p_0}}\right).$$

The Boltzmann factors $\exp(-E_{x_j}/kT)$ have canceled out. So, at high enough temperatures for the narrow resonance formalism to hold, the only temperature dependence of the effect of the excited states in the entrance channel is the weak influence of the quantity $(2J_0+1)/Z$. The effect of the thermal population of the excited states is important if the partial proton widths to these states are substantial, relative to the partial proton width for decay to the ground state. The shell-model estimates of Table II show that this could be the case especially for the 661 keV resonance and this would imply an enhancement of its contribution to the reaction rate already from temperatures of 4×10^8 K on.

VI. ASTROPHYSICAL IMPLICATIONS

In order to assess the implications of the $^{19}\mathrm{Ne}(p,\gamma)$ reaction rate one has to compare with the preceding step in the $^{15}\mathrm{O}(\alpha,\gamma)\,^{19}\mathrm{Ne}(p,\gamma)$ reaction sequence. More precisely, the respective regions in a (density,temperature)-phase diagram in which each reaction is faster than the decay of the nucleus in the entrance channel have to be delineated and compared:

$$\lambda_{\mathrm{reaction}} \geqslant \lambda_{\mathrm{decay}}.$$

$\lambda_{\mathrm{reaction,decay}}$ are called destruction rates and are given by

$$\lambda_{\mathrm{reaction}} = \frac{X}{A}\rho N_A \langle \sigma v \rangle,$$

$$\lambda_{\mathrm{decay}} = \frac{\ln 2}{T_{1/2}}.$$

Here X is the mass fraction of the captured isotope and A its mass in atomic mass units. We assumed solar mass fractions for hydrogen and helium: $X_{\mathrm{H}}=0.71$ and $X_{\mathrm{He}}=0.27$ [52]. ρ is the mass density of the stellar plasma. In the evaluation of the $^{15}\mathrm{O}(\alpha,\gamma)\,^{19}\mathrm{Ne}$ rate we considered resonances with $l \leqslant 3$: at 504 keV [$\omega\gamma=(20\pm3)\mu$ eV [9]], 850 keV [$\omega\gamma=(11\pm8)$ meV [10]], 1020 keV [$\omega\gamma=(6.3\pm3.5)$ meV [10]], 1071 keV [$\omega\gamma=(187\pm48)$ meV [10]], and 1183 keV [$\omega\gamma=(113\pm17)$ meV [53]]. The resonance strengths from Ref. [10] are deduced from the Γ_α/Γ ratios from Ref. [53]. Therefore we adopted the relative errors from Ref. [53]. The DC rate is taken from Ref. [29], but is only important below 1×10^8 K. The division between reaction-dominated (higher temperature and density) and decay-dominated regions is indicated for both reactions in the phase diagram of Fig. 1. Also indicated are typical values for density and temperature of various astrophysical sites that have been proposed as locations of explosive hydrogen burning [1–3].

At first sight one would conclude that the $^{15}\mathrm{O}(\alpha,\gamma)\,^{19}\mathrm{Ne}$ reaction clearly is the bottleneck for the breakout from the hot CNO cycle into the rp process. However, as the Q value of the $^{19}\mathrm{Ne}(p,\gamma)$ is only 2.195 MeV the photodisintegration of the produced $^{20}\mathrm{Na}$ nuclei will be considerable at high temperatures and may impede and eventually stop the flow of nuclear matter to higher masses. Due to the higher Q value of 3.53 MeV of the $^{15}\mathrm{O}(\alpha,\gamma)\,^{19}\mathrm{Ne}$ reaction the first step in the $^{15}\mathrm{O}(\alpha,\gamma)\,^{19}\mathrm{Ne}(p,\gamma)\,^{20}\mathrm{Na}$ sequence will be much less exposed to effects of photodisintegration of $^{19}\mathrm{Ne}$.

The destruction rate of the $^{20}\mathrm{Na}$ nuclei by photodisintegration follows from the principle of detailed balance [54]:

$$\lambda_{^{20}\mathrm{Na}(\gamma,p)} = \frac{2Z_{^{19}\mathrm{Ne}}}{Z_{^{20}\mathrm{Na}}}\left(\frac{m_{^{19}\mathrm{Ne}}m_p kT}{m_{^{20}\mathrm{Na}}2\pi\hbar^2}\right)^{3/2}\langle\sigma v\rangle_{^{19}\mathrm{Ne}(p,\gamma)}\exp(-Q/kT).$$

For a density of 0.71×10^4 g/cm^3 the destruction rate of $^{20}\mathrm{Na}$ by photodisintegration equals the destruction rate of $^{19}\mathrm{Ne}$ by proton capture already at 1.7×10^9 K.

Ideally, if the $^{20}\mathrm{Na}$ nuclei were only destroyed by photodisintegration, for each temperature and density a (p,γ)-(γ,p) equilibrium would be achieved that would be reflected in the ratio of the respective abundances:

$$\frac{Y_{^{20}\mathrm{Na}}}{Y_{^{19}\mathrm{Ne}}} = \frac{\lambda_{^{19}\mathrm{Ne}(p,\gamma)}}{\lambda_{^{20}\mathrm{Na}(\gamma,p)}}. \tag{15}$$

In reality the $^{20}\mathrm{Na}$ nuclei are also consumed by β^+ decay and by proton capture leading to $^{21}\mathrm{Mg}$. Then the (p,γ)-(γ,p) equilibrium of Eq. (15) will be established if the photodisintegration is sufficiently rapid:

$$\lambda_{^{20}\mathrm{Na}(\gamma,p)} \geqslant \lambda_{^{20}\mathrm{Na}(p,\gamma)} + \lambda_{^{20}\mathrm{Na}(\beta^+\nu)}. \tag{16}$$

The region of the phase diagram in which this condition is fulfilled is presented in Fig. 2 as a gray area. The dark gray band indicates the uncertainty due to the uncertainty on our $^{19}\mathrm{Ne}(p,\gamma)\,^{20}\mathrm{Na}$ reaction rate. The $^{20}\mathrm{Na}(p,\gamma)\,^{21}\mathrm{Mg}$ reaction rate was calculated according to Ref. [55].

In equilibrium conditions the destruction of the $^{20}\mathrm{Na}$ nuclei by decay or proton capture acts through the (p,γ)-(γ,p) equilibrium of Eq. (15) on the $^{19}\mathrm{Ne}$ nuclei and leads to an effective destruction rate of $^{19}\mathrm{Ne}$ nuclei to higher masses $\lambda^{\mathrm{eff}}_{^{19}\mathrm{Ne}}$ [3]:

$$\begin{aligned}
(\lambda_{^{20}\mathrm{Na}(p,\gamma)} + \lambda_{^{20}\mathrm{Na}(\beta+\nu)})Y_{^{20}\mathrm{Na}} &= \left(\lambda_{^{20}\mathrm{Na}(p,\gamma)} + \lambda_{^{20}\mathrm{Na}(\beta\nu)}\frac{Y_{^{20}\mathrm{Na}}}{Y_{^{19}\mathrm{Ne}}}\mathrm{Y}_{^{19}\mathrm{Na}}\right.\\
&= \left.\lambda_{^{20}\mathrm{Na}(\beta^+\nu)}\right)\frac{\lambda_{^{19}\mathrm{Ne}(p,\gamma)}}{\lambda_{^{20}\mathrm{Na}(\gamma,p)}}Y_{^{19}\mathrm{Ne}}\\
&\equiv \lambda^{\mathrm{eff}}_{^{19}\mathrm{Ne}}Y_{^{19}\mathrm{Ne}}.
\end{aligned} \tag{17}$$

If the effective destruction of the $^{19}\mathrm{Ne}$ nuclei to higher masses is slower than its β^+ decay, then the nuclear matter flow to the rp-process region will be impeded. So $^{19}\mathrm{Ne}$ will act as a waiting point if the following condition is fulfilled:

$$\lambda_{^{19}\mathrm{Ne}(\beta^+\nu)} \geqslant \lambda^{\mathrm{eff}}_{^{19}\mathrm{Ne}}.$$

The region in the phase diagram where $^{19}\mathrm{Ne}$ is a waiting point due to the photodisintegration of $^{20}\mathrm{Na}$ is delineated by a full line in Fig. 2. In order to check the sensitivity to the precise value of the $^{20}\mathrm{Na}(p,\gamma)\,^{21}\mathrm{Mg}$ reaction rate we did the calculation taking into account only the β^+ decay of $^{20}\mathrm{Na}$ in the evaluation of $\lambda^{\mathrm{eff}}_{^{19}\mathrm{Ne}}$ [Eq. (17)]. The resulting region is delineated by a dashed line in Fig. 2. We conclude that for realistic densities and temperatures the photodisintegration will not hinder the transition from the CNO cycle to the rp process.

VII. CONCLUSIONS

The population of the lowest resonances in $^{20}\mathrm{Na}$ has been studied in the measurement of the $^{19}\mathrm{Ne}(p,\gamma)\,^{20}\mathrm{Na}$ reaction using radioactive $^{19}\mathrm{Ne}$ beams and with the help of three different detection setups. Limits on the resonance strengths have been deduced and compared with theoretical estimates which we have consistently calculated in the framework of the shell model. Both upper and lower limits on the resonant component of the $^{19}\mathrm{Ne}_{\mathrm{g.s.}}(p,\gamma)\,^{20}\mathrm{Na}$ reaction rate have been deduced on the basis of our experimental results.

We have also measured the ^{19}Ne(d,n)^{20}Na excitation curve between 0.6 and 1.8 MeV in the center-of-mass frame. The subsequent DWBA analysis using shell-model spectroscopic factors and the comparison with the ^{19}F(d,p)^{20}F reaction indicate that the difference between calculated and observed cross section would be due to contributions from the compound nucleus mechanism. We have calculated the DC rate of the ^{19}Ne$_{\text{g.s.}}(p,\gamma)$^{20}Na reaction in the framework of a potential model and scaled by the shell-model values of the spectroscopic factors.

The astrophysical implications of the resulting total astrophysical reaction rate have been investigated. The conditions for the breakout from the hot CNO cycle to the rp process will be determined by the preceding ^{15}O(α,γ)^{19}Ne reaction. The photodisintegration of ^{20}Na will not hinder the breakout. In view of this conclusion it is worthwhile to determine the ^{15}O(α,γ)^{19}Ne reaction rate in a direct experimental way.

ACKNOWLEDGMENTS

The authors thank the cyclotron crew at Louvain-la-Neuve for efficiently running the RIB facility and Dr. H. Vanmarcke and P. Willeborts for etching the SSNTD's at the SCK, Mol, Belgium. F.B., P.L., and J.V. acknowledge FNRS, Belgium. G.V. acknowledges NFWO, Belgium. M.G. acknowledges the Belgian IWT. This text presents the research results of the Belgian program on Interuniversity Poles of Attraction, initiated by the Belgian state, Federal Services of Scientific, Technical and Cultural Affairs and was also supported by the UK EPSRC. H.H. and H.O. thank the Fonds zur Förderung der Wissenschaftlichen Forschung in Österreich (Project No. S7307-AST) for financial support. Scientific responsibility is assumed by the authors.

---

[1] R. Wallace and S. E. Woosley, Astrophys. J., Suppl. Ser. **45**, 389 (1981).

[2] A. E. Champagne and M. Wiescher, Annu. Rev. Nucl. Part. Sci. **42**, 39 (1992).

[3] L. Van Wormer, J. Görres, C. Iliadies, M. Wiescher, and F.-K. Thielemann, Astrophys. J. **432**, 326 (1994).

[4] K. E. Rehm *et al.*, Phys. Rev. C **53**, 1950 (1996).

[5] M. Wiescher and K. U. Kettner, Astrophys. J. **263**, 891 (1982).

[6] J. Görres, M. Wiescher, and F.-K. Thielemann, Phys. Rev. C **51**, 392 (1995).

[7] M. A. J. Snijders, T. J. Batt, M. J. Seaton, J. C. Blades, and D. C. Morton, Mon. Not. R. Astron. Soc. **211**, 7 (1984); R. E. Williams, E. P. Ney, W. M. Sparks, S. G. Starrfield, J. W. Truran, and S. Wyckoff, *ibid.* **212**, 753 (1985).

[8] R. E. Williams and J. S. Gallagher, Astrophys. J. **228**, 482 (1979).

[9] Z. Q. Mao, T. H. Fortune, and A. G. Lacaze, Phys. Rev. Lett. **74**, 3760 (1995); Phys. Rev. C **53**, 1197 (1996).

[10] S. Wilmes, P. Mohr, U. Atzrott, V. Kölle, G. Staudt, A. Mayer, and W. Hammer, Phys. Rev. C **52**, R2823 (1995).

[11] J. Görres and M. Wiescher, Phys. Rev. C **52**, 412 (1995), and references therein.

[12] R. Coszach *et al.*, Phys. Rev. C **50**, 1695 (1994).

[13] L. O. Lamm, C. P. Browne, J. Görres, S. M. Graff, M. Wiescher, A. A. Rollefson, and B. A. Brown, Nucl. Phys. **A510**, 503 (1990).

[14] S. Kubono *et al.*, Z. Phys. A **331**, 359 (1988).

[15] S. Kubono, H. Orihara, S. Kato, and T. Kajino, Astrophys. J. **344**, 460 (1989).

[16] S. Kubono *et al.*, Phys. Rev. C **46**, 361 (1992).

[17] J. Görres, M. Wiescher, K. Scheller, D. J. Morrissey, B. M. Sherrill, D. Bazin, and J. A. Winger, Phys. Rev. C **46**, R833 (1992).

[18] A. Piechaczek *et al.*, Nucl. Phys. **A584**, 509 (1995).

[19] B. A. Brown, A. E. Champagne, H. T. Fortune, and R. Sherr, Phys. Rev. C **48**, 1456 (1993).

[20] L. O. Lamm, C. P. Browne, J. Görres, M. Wiescher, and A. A. Rollefson, Z. Phys. A **327**, 239 (1987).

[21] M. S. Smith, P. V. Magnus, K. I. Hahn, A. J. Howard, P. D. Parker, A. E. Champagne, and Z. Q. Mao, Nucl. Phys. **A536**, 333 (1992).

[22] N. M. Clarke, P. R. Hayes, M. B. Becha, C. N. Pinder, and S. Roman, J. Phys. G **16**, 1547 (1990).

[23] B. D. Anderson *et al.*, Phys. Rev. C **43**, 50 (1991): B. D. Anderson *et al.*, *ibid.* **52**, 2210 (1995).

[24] D. E. Alburger, G. Wang, and E. K. Warburton, Phys. Rev. C **35**, 1479 (1987).

[25] P. Descouvemont and D. Baye, Nucl. Phys. **A517**, 143 (1990).

[26] E. K. Warburton and B. A. Brown, Phys. Rev. C **46**, 923 (1992).

[27] S. Raman, E. K. Warburton, J. W. Starner, E. T. Jurney, J. E. Lynn, P. Tikkanen, and J. Keinonen, Phys. Rev. C **53**, 616 (1996).

[28] N. M. Clarke, S. Roman, C. N. Pinder, and P. R. Hayes, J. Phys. G **19**, 1411 (1993).

[29] K. Langanke, M. Wiescher, W. A. Fowler, and J. Görres, Astrophys. J. **301**, 629 (1986).

[30] C. Rolfs, Nucl. Phys. **A217**, 29 (1973).

[31] R. D. Page *et al.*, Phys. Rev. Lett. **73**, 3066 (1994).

[32] C. Michotte *et al.*, Phys. Lett. B **381**, 402 (1996).

[33] G. Vancraeynest *et al.*, in *Proceedings of the Fourth International Conference on Radioactive Nuclear Beams, Omiya, Japan, 1996* [Nucl. Phys. **A616**, 107c (1997)].

[34] C. Michotte, J.-S. Graulich, Th. Delbar, P. Leleux, and P. Lipnik, Nucl. Instrum. Methods Phys. Res. A **366**, 155 (1995).

[35] G. Vancraeynest, S. Franchoo, M. Huyse, and R. Moons, Nucl. Instrum. Methods Phys. Res. B **129**, 65 (1997).

[36] G. F. Knoll, *Radiation Detection and Measurement* (Wiley, New York, 1979), p. 42.

[37] V. M. Zabegai, A. E. Melenevskii, D. F. Nemetz, V. N. Nemykin, Yu. S. Stryuk, and K. O. Teretskii, Sov. J. Nucl. Phys. **10**, 2 (1970).

[38] W. Galster *et al.*, Phys. Rev. C **44**, 2776 (1991).

[39] H. Oberhummer and G. Staudt, in *Nuclei in the Cosmos*, edited by H. Oberhummer (Springer-Verlag, Berlin, New York, 1991), p. 29.

[40] A. M. Kobos, B. A. Brown, R. Lindsay, and G. R. Satchler, Nucl. Phys. **A425**, 205 (1984).

[41] H. de Vries, C. W. de Jager, and C. de Vries, At. Data Nucl. Data Tables **36**, 495 (1987).

[42] B. A. Brown, A. Etchegoyen, W. D. M. Rae, and N. S. Godwin, code OXBASH, 1984 (unpublished).

[43] H. T. Fortune and R. R. Betts, Phys. Rev. C **10**, 1292 (1974).

[44] M. Carchidi, B. H. Wildenthal, and B. A. Brown, Phys. Rev. C **34**, 2280 (1986).

[45] B. A. Brown and B. H. Wildenthal, Nucl. Phys. **A474**, 290 (1987).

[46] M. E. O. de Lopez, J. Richards, and M. Mazari, Nucl. Phys. **51**, 321 (1964).

[47] M. N. H. Comsan, A. A. El-Kamhawy, F. Asfour, and M. Abd-El-Fattah, Atomkernenergie **26**, 37 (1975).

[48] S. Laribi, H. Beaumevieille, N. Bendjaballah, D. Lalanne, J. F. Allard, and B. Faid, Nucl. Phys. **A191**, 368 (1972).

[49] V. F. Sears, Neutron News **3**, 26 (1992).

[50] H. Feshbach, in *Nuclear Spectroscopy*, edited by F. Azjenberg-Selove (Academic, New York, 1960), Pt. B, p. 660.

[51] W. A. Fowler, G. R. Caughlan, and B. A. Zimmerman, Astron. Astrophys. **13**, 69 (1975).

[52] E. Anders and N. Grevesse, Geochim. Cosmochim. Acta **53**, 197 (1989).

[53] P. V. Magnus, M. S. Smith, A. J. Howard, P. D. Parker, and A. E. Champagne, Nucl. Phys. **A506**, 332 (1990).

[54] W. A. Fowler, G. R. Caughlan, and B. A. Zimmerman, Annu. Rev. Astron. Astrophys. **5**, 525 (1967).

[55] S. Kubono *et al.*, Nucl. Phys. **A537**, 153 (1992).